

Platform Motion Effects on Measurements of Turbulence and Air–Sea Exchange over the Open Ocean

SCOTT D. MILLER

Atmospheric Sciences Research Center, University at Albany, State University of New York, Albany, New York

TIHOMIR S. HRISTOV

Civil Engineering Department, The Johns Hopkins University, Baltimore, Maryland

JAMES B. EDSON

Marine Sciences Department, University of Connecticut-Avery Point, Groton, Connecticut

CARL A. FRIEHE

Mechanical and Aerospace Engineering Department, University of California, Irvine, Irvine, California

(Manuscript received 22 December 2006, in final form 3 February 2008)

ABSTRACT

Platform motion contaminates turbulence statistics measured in the surface layer over the ocean and therefore adds uncertainty to the understanding and parameterization of air–sea exchange. A modification to the platform motion–correction procedure of Edson et al. is presented that explicitly accounts for misalignment between anemometers and motion sensors. The method is applied to a high-resolution dataset, including four levels of turbulence within 20 m of the ocean surface, measured over deep ocean waves using the stable research platform R/P *FLIP*. The average error magnitude of the air–sea momentum flux (wind stress) from the four sensors during a 6-day period (10-m wind speed 2–14 m s⁻¹) was 15% ± 1%, and varied systematically with measurement height. Motion and sensor-mounting offsets caused wind stress to be underestimated by 15% at 18.1 m, 13% at 13.8 m, and 11% at 8.7 m, and to be overestimated by 3% at 3.5 m. Sensor misalignment contributed to one-third of the correction to the wind stress. The motion correction reduced some measured artifacts in the wind that could otherwise be interpreted in terms of air–sea interaction, such as the angle between wind and wind stress vectors, while other features remained in the corrected wind, such as apparent upward momentum transfer from ocean to the atmosphere during low wind. These results demonstrate the complex interaction between motion and wind turbulence, and reinforce the necessity to measure and correct for platform motion. Finally, it is shown that the effects of motion on wind stress measured using R/P *FLIP* are much smaller than in situ measurements made using a conventional research ship.

1. Introduction

The motion of ships and buoys at sea represents a major source of uncertainty in measurements of turbulence and air–sea interaction in the marine atmospheric surface layer. The three-dimensional wind velocity measured by an anemometer fixed to a moving plat-

form includes spurious contributions due to pitch, roll, heave, yaw, and translation. The apparent wind induced by motion contaminates turbulence statistics, including correlations such as wind stress (the exchange of momentum between the atmosphere and ocean surface), one of the most important couplings between the air and sea. Nonetheless, direct flux measurements at sea can provide important insight into the air–sea momentum flux that generates ocean waves, drives ocean currents, provides energy for ocean mixing, and generates storm surge. While most air–sea momentum exchange is downward to the surface and occurs via tur-

Corresponding author address: Scott D. Miller, Atmospheric Sciences Research Center, State University of New York at Albany, 251 Fuller Road L317, Albany, NY 12203.
E-mail: smiller@albany.edu

TABLE 1. Summary of platform motion corrections reported for wind measured from ships and buoys, including platform type, motion measurement system, sensors used, and the effect of motion on wind stress (where available).

Reference	Platform	Measurement system	Sensors	Effect on wind stress
Dunckel et al. (1974)	Buoy, open ocean	Gyrostabilized	Three accelerometers	Underestimated stress 40%
Leavitt and Paulson (1975)	R/P <i>FLIP</i> , open ocean	Strapdown	Three accelerometers	Not reported
Schmitt et al. (1979)	R/P <i>FLIP</i> , open ocean	Gyros	Gyroscope	Not reported
Fujitani (1985)	Ship, open ocean	Gyros	Three accelerometers	Not reported
Dugan et al. (1991)	Buoy, seaway	Gimbaled	Accelerometers	Not measured
Ancil et al. (1994)	Buoy	Gimbaled	Accelerometers	Not reported
Song et al. (1996)	Ship, open ocean	Strapdown	Six-accelerometer array	Not reported
Edson et al. (1998)	Ship, catamaran, open ocean	Strapdown	Three accelerometers, three rate sensors	Overestimated stress*
Schulz et al. (2005)	Ship, coastal ocean	Strapdown	Six-accelerometer array	Underestimated stress 4%–20%

* E98 compared wind stress measured from two platforms with estimates based on bulk formulas before and after correction (their Figs. 10–13) and concluded that the measured wind stress was overestimated but did not give the magnitude of the overestimate.

bulent transport, more subtle yet important interactions exist, such as wave-correlated perturbations in the wind that provide momentum and energy to grow ocean waves (Hristov et al. 2003), reverse (upward) momentum transfer during light winds with running waves (Grachev and Fairall 2001), swell effects on the drag coefficient (Drennan et al. 1999), and the angle between wind and wind stress vectors (Geernaert et al. 1993; Rieder et al. 1994; Friehe et al. 2001, Grachev et al. 2003). To obtain the air–sea momentum flux and extract these couplings, the contribution of platform motion to the measurements of the fluctuating wind vector must be carefully removed.

Several techniques have been used to correct the three-dimensional wind vector measured at sea for the effects of platform motion. Table 1 summarizes previous studies that considered the effects of motion on measured wind velocity. Besides Dunckel et al. (1974) who used real-time active control to maintain the orientation of an instrumented buoy, passive approaches have most commonly been used, whereby the instantaneous measured wind vector is rotated to an earth coordinate frame using measured or calculated instantaneous pitch and roll angles. The pitch and roll angles are directly returned by gyros, similar to systems used on aircraft platforms (Fujitani 1985), or can be calculated from less-expensive “strapped-down” systems that are fixed to the platform. Strapped-down systems consisting of either sets of six accelerometers (e.g., Song et al. 1996; Schulz et al. 2005) or three orthogonal angle rate sensors and three orthogonal linear accelerometers (e.g., Edson et al. 1998, hereafter E98) have been reported. The few reports that quantify the effect of platform motion on wind stress demonstrate that it can be a large fraction of the true momentum flux

(Table 1), some finding that platform motion caused wind stress to be underestimated (e.g., Dunckel et al. 1974; Schulz et al. 2005) and others overestimated (e.g., E98). To date, no studies have reported the effect of motion corrections on wind and turbulence measured by multiple, spatially separated sensors fixed to the same platform.

An issue that has not been considered explicitly in the motion correction of turbulence measurements over the ocean is the effect of mounting misalignment between the three-dimensional anemometer and three-dimensional motion sensor coordinate systems. Misalignment between the motion sensor and anemometer coordinate frames can introduce errors that propagate through the motion-correction scheme and affect the resulting turbulent statistics. The issue of sonic anemometer orientation has recently received some attention (Wilczak et al. 2001; Vickers and Mahrt 2006). E98 avoided mounting offsets between the sonic and motion sensor by collocating and rigidly fixing the motion sensor to the anemometer, such that the two coordinate systems were coaligned. However, coalignment may not be possible in cases where the motion sensor and anemometer are not rigidly fixed to one another. For example, some approaches to measuring motion use a distributed array of accelerometers that are mounted separately from the anemometer (e.g., Song et al. 1996; Schulz et al. 2005).

In this paper, we expand the analysis of E98 to include the effect of misalignment between the anemometer and motion sensor coordinate frames in the motion-correction equation. We present a method for estimating the misalignment of the coordinate axes by using long-term records of the measured motion sensor and anemometer signals to calculate their mean orien-

tations, similar to the “planar fit” presented by Wilczak et al. (2001). We also present refinements of the motion corrections detailed in E98 with regard to the selection of digital filters used to calculate the transformation matrix and to integrate accelerometers. The corrections are applied to a high-resolution dataset obtained using the stable research platform R/P *FLIP* (Fig. 1; Rudnick 1967), which included measurements of the turbulent wind vector at four heights within 20 m of the ocean surface above deep waves. We show the variations in the effect of platform motion on turbulence statistics and spectra measured by the spatially separated sensors, and demonstrate the importance of sensor misalignment between anemometer and motion sensor. We also show that motion correction can change the qualitative interpretation of the wind–wave coupling, such as the presence of upward momentum transfer from waves to wind, and the wind stress angle. Finally, we compare motion corrections for the *FLIP* dataset with those from a conventional ocean research vessel, the R/V *Wecoma*, measured in situ.

2. Methods

a. Motion-correction equation

We define three right-handed coordinate frames. The earth-reference frame (subscript *e*) is defined with *x* axis eastward, *y* axis northward, and *z* axis up. The origin of this frame translates with the ship. The platform frame (subscript *p*) is defined by the instantaneous location and orientation of the three orthogonal motion sensor coordinate axes. Similarly, the anemometer frame (subscript *a*) is defined by the instantaneous location and orientation of the three orthogonal sonic anemometer coordinate axes. The platform and anemometer coordinate frames translate, pitch, roll, yaw, and heave with the platform, with *x* axis (nominally) toward the bow and *y* axis toward port (Fig. 1). For a right-handed system, positive roll refers to portside up, positive pitch refers to bow down, and positive yaw refers to counterclockwise rotation.

A vector **a** in coordinate frame α is denoted \mathbf{a}_α . This vector is transformed to coordinate frame β by multi-

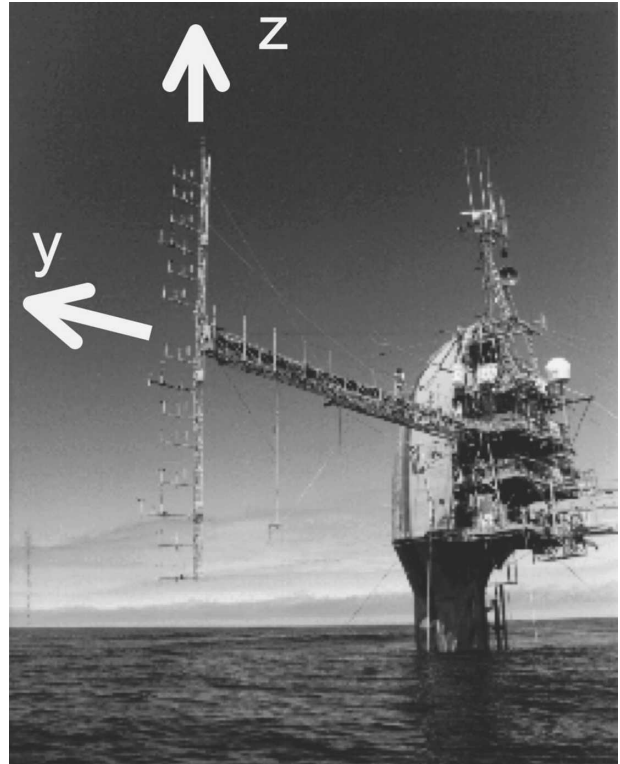


FIG. 1. The research platform R/P *FLIP*. To optimize instrument exposure, *FLIP* was set in a three-point mooring in water of 1500-m depth and maintained a keel heading of $350^\circ \pm 15^\circ$ true, into the climatological wind direction. Sonic anemometers were mounted on the mast at the end of the 20-m-long portside boom, at 8.7, 13.8, and 18.1 m above the ocean surface; a fourth sonic anemometer was hung upside-down ~5 m inward of the mast and 3.5 m above the ocean surface. The right-handed platform coordinate frame is indicated by the vertical (*z*) and portward (*y*) arrows; the *x* axis points keelward.

plication with the rotation matrix $\mathbf{T}_{\beta\alpha}$; that is, $\mathbf{a}_\beta = \mathbf{T}_{\beta\alpha}\mathbf{a}_\alpha$. A coordinate transformation can be defined by three Euler angles (ϕ, θ, ψ) as $\mathbf{T}_{\beta\alpha} = [\psi_{\beta\alpha}][\theta_{\beta\alpha}][\phi_{\beta\alpha}]$, where the first rotation is about the *x* axis (roll ϕ), the second rotation is about the intermediate *y* axis (pitch θ), and the final rotation is about the new intermediate *z* axis (yaw, or heading, ψ), and the square brackets denote rotation matrices. The individual rotations are expressed in matrix form as

$$[\phi_{\beta\alpha}] = \begin{bmatrix} 1 & 0 & 0 \\ 0 & \cos\phi_{\beta\alpha} & -\sin\phi_{\beta\alpha} \\ 0 & \sin\phi_{\beta\alpha} & \cos\phi_{\beta\alpha} \end{bmatrix}, \quad [\theta_{\beta\alpha}] = \begin{bmatrix} \cos\theta_{\beta\alpha} & 0 & \sin\theta_{\beta\alpha} \\ 0 & 1 & 0 \\ -\sin\theta_{\beta\alpha} & 0 & \cos\theta_{\beta\alpha} \end{bmatrix}, \quad [\psi_{\beta\alpha}] = \begin{bmatrix} \cos\psi_{\beta\alpha} & -\sin\psi_{\beta\alpha} & 0 \\ \sin\psi_{\beta\alpha} & \cos\psi_{\beta\alpha} & 0 \\ 0 & 0 & 1 \end{bmatrix}. \quad (1)$$

The true wind vector, $\mathbf{u} = (u_{\text{east}}, u_{\text{north}}, w)$, is the sum of the apparent wind vector measured by the anemometer and expressed in the anemometer frame \mathbf{u}_a and the

velocity of the anemometer expressed in the platform frame, $\mathbf{v}_p + \mathbf{v}_{\text{ship}}$, where \mathbf{v}_p is the velocity of the anemometer due to ship motions (pitch, roll, yaw, and

TABLE 2. Location of sonic anemometers relative to motion sensor, and mean tilt (equivalent roll and pitch angles in degrees) of the motion sensor and sonic anemometers for the R/P *FLIP* dataset. Two intervals during the campaign are distinguished, before (interval 1) and after (interval 2) the mast was struck by waves and caused the mean offsets to change.

	Location relative to motion sensor			Equivalent ϕ roll		Equivalent θ pitch	
	X	Y	Z	Interval 1	Interval 2	Interval 1	Interval 2
Motion Pak	0	0	0	2.4	2.1	1.8	3.2
18.1 m	0	0	7.5	-0.7	-0.1	-0.2	1.4
13.8 m	0	1.4	3.1	0.9	0.4	1.5	2.8
8.7 m	0	1.4	-1.9	1.2	-0.8	1.5	3.8
3.5 m	0	-3.7	-7.0	2.4	2.7	4.3	6.7

heave), and \mathbf{v}_{ship} is the velocity of the ship recorded by the ship's navigation system or a GPS receiver. Expressing all terms in the *earth coordinate frame*,

$$\mathbf{u} = \mathbf{T}_{ea}\mathbf{u}_a + \mathbf{T}_{ep}\mathbf{v}_p + \mathbf{v}_{\text{ship}}, \quad (2)$$

where the transformation \mathbf{T}_{ea} rotates the wind vector measured in the anemometer's frame to the earth frame, and \mathbf{T}_{ep} rotates the velocity of the anemometer measured in the platform frame to the earth frame. Note that if the anemometer and platform (i.e., motion sensor) coordinate axes are collinear, $\mathbf{T}_{ea} = \mathbf{T}_{ep}$.

Following E98, we focus on strapped-down motion sensors that measure three linear accelerations and three angle rates. It is convenient to separate the anemometer velocity (\mathbf{v}_p) into linear and angular motion terms, $\mathbf{v}_p = \int \ddot{\mathbf{x}}_p dt + \boldsymbol{\Omega}_p \times \mathbf{r}_p$, where $\ddot{\mathbf{x}}_p = (\ddot{x}_p, \ddot{y}_p, \ddot{z}_p)$ is linear acceleration, $\boldsymbol{\Omega}_p = (\omega_x, \omega_y, \omega_z)$ is the angular velocity vector, and $\mathbf{r}_p = (x_p, y_p, z_p)$ is the position vector from the motion sensor to the anemometer. We assume that \mathbf{r}_p is known and constant, and Eq. (2) becomes

$$\mathbf{u} = \mathbf{T}_{ea}\mathbf{u}_a + \mathbf{T}_{ep} \left(\int \ddot{\mathbf{x}}_p dt + \boldsymbol{\Omega}_p \times \mathbf{r}_p \right) + \mathbf{v}_{\text{ship}}. \quad (3)$$

Equation (3) is analogous to E98, except that for their mounting arrangement the anemometer and motion sensor axes were collinear so that $\mathbf{T}_{ea} = \mathbf{T}_{ep}$.

b. Measurements from R/P *FLIP* and R/V *Wecoma*

We focus on data collected using the research platform R/P *FLIP*, a 120-m-long spar buoy designed for stability in the vertical orientation (Fig. 1). *FLIP* was moored 50 km off the coast of California (water depth 1500 m) for 12 days during the marine boundary layer (MBL) experiment in spring 1995 (27 April–9 May, days of year 117–128.5). A three-point mooring maintained a keel heading of $350^\circ \pm 15^\circ$, and *FLIP* remained in a fixed location such that $\mathbf{v}_{\text{ship}} = 0$ in Eq. (3). A 16-m-long vertical mast (triangular cross section with 23-cm side length) was fixed to the end of *FLIP*'s port-

side boom by a hinge mechanism that allowed the mast to pivot horizontal for installation of sensors (Fig. 1). The nominal x axis of the motion sensor and anemometer coordinate frames pointed to *FLIP*'s keel, and the nominal y axis outward along the portside boom.

The turbulent wind velocity plus contributions due to motion, $\mathbf{u}_a + \mathbf{v}_p + \mathbf{v}_{\text{ship}}$, was measured using four three-dimensional ultrasonic (sonic) anemometers (Model 1012, Gill Instruments, Ltd., Great Britain). Three sonics were mounted along the vertical mast at the end of *FLIP*'s portside boom, at 8.7, 13.8, and 18.1 m above the mean ocean surface. Each sonic was mounted to a 3.8-cm-diameter aluminum pipe that extended 2 m from the vertical mast in the portward direction. A fourth sonic was hung upside-down from the port boom using a 5.1-cm-diameter aluminum pipe, approximately 5 m inward from the mast and 3.5 m above the mean ocean surface. The alignment of the three sonic anemometers fixed to the mast was sighted by eye, while the mast lay flat on the portside boom. The mast was then pivoted to the vertical position, as shown in Fig. 1.

Motion was measured using a 6-degrees-of-freedom inertial sensor (Systron-Donner MotionPak) mounted at the end of the portside boom at the hinge point of the mast. The motion sensor consisted of three orthogonal linear accelerometers (to measure $\ddot{\mathbf{x}}_p$, resolution $<10 \mu\text{g}$) and three orthogonal angle rate sensors (to measure $\boldsymbol{\Omega}_p$, resolution $<0.004^\circ \text{ s}^{-1}$), and was the same unit used by E98. The locations of the anemometers mounted to the vertical mast relative to the motion sensor are listed in Table 2. *FLIP*'s compass heading was recorded by the ship gyroscope. Wind and motion data were recorded at 50 Hz and subsequently resampled to 5 Hz for processing.

To demonstrate the effectiveness of *FLIP* for making wind and wind stress measurements, we compared the *FLIP* data with in situ data collected from the R/V *Wecoma*, a 56-m-long conventional research vessel that operated near *FLIP* during the 1995 MBL campaign. The wind vector and ship motion were measured by sensors at *Wecoma*'s bow, approximately 10 m above

the mean ocean surface. A critical difference between the *FLIP* and *Wecoma* datasets was that, for *Wecoma*, the relative mounting between the motion sensor and anemometer was fixed using a machined mounting bracket. Because of the fixed alignment of the anemometer and motion sensor, there was no correction required for misalignment between the two sensors for the *Wecoma* data [i.e., $\mathbf{T}_{ea} = \mathbf{T}_{ep}$ in Eq. (3)]. Therefore, the comparison between motion corrections for the *FLIP* and *Wecoma* datasets demonstrates the sensitivity to different amounts of motion experienced by different platforms measuring in situ during the same wind and wave conditions. The comparison of the importance of accounting for sensor misalignment will be presented by comparing motion corrections with and without accounting for the mounting offsets using data collected from the four sensors on *FLIP*.

c. The transformation matrix

The procedure for calculating the transformation \mathbf{T}_{ep} was detailed by E98. To summarize, the time-dependent Euler angles were calculated in two ways: the first is based on integration of the angle rate sensors and the second on the ratio of measured horizontal acceleration components to the gravity acceleration, \mathbf{g} , $\phi \approx \tan^{-1}(\dot{y}_p/g)$ and $\theta \approx \tan^{-1}(-\dot{x}_p/g)$. The two estimates were combined using complimentary filtering, where high-pass-filtered rate-sensor-based angle estimates were combined with low-pass-filtered estimates from the accelerometers. We used a fourth-order Butterworth filter to define the complementary filter, with a cutoff period of 50 s, and the filter was applied forward and backward on each motion channel to eliminate phase shifts (e.g., Oppenheim and Schaffer 1989). We found that the use of a higher-order filter than the first-order filter used in E98 (and that corresponds to the definition of the complimentary filter) resulted in less “leakage” between the angle-rate-sensor-based and accelerometer-based Euler angle estimates. The low-frequency yaw was obtained from a gyro on *FLIP* and from the GPS receiver on R/V *Wecoma*, and \mathbf{T}_{ep} was calculated as the matrix product of the individual rotations, $\mathbf{T}_{ep} = [\psi_{ep}][\theta_{ep}][\phi_{ep}]$.

The platform linear velocity was calculated by integrating the linear accelerations in the earth frame, $\int \mathbf{T}_{ep} \ddot{\mathbf{x}}_p dt$. The numerical integration amplified low-frequency drift of the accelerometers, and high-pass filtering was necessary after integrating (also observed by E98). The filter cutoff period was selected empirically by plotting velocity variances and covariances versus a range of values for the filter cutoff, and by choosing values at which statistics became insensitive to further increases in cutoff period (Fig. 2). The filter cutoff pe-

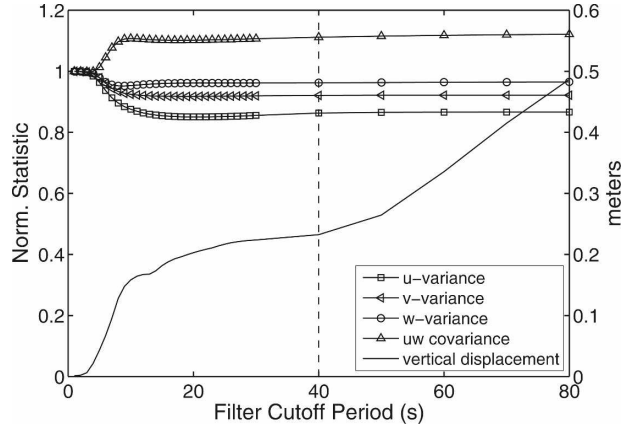


FIG. 2. Effect of accelerometer filter-cutoff period on calculated wind statistics and platform displacement measured from R/P *FLIP*, for a 30-min data interval. Normalized 8.7-m wind velocity statistics: u variance, squares; v variance, left-facing triangles; w variance, circles; and uw covariance, upward-facing triangles. The range of calculated vertical displacement (m) at the end of *FLIP*'s portside boom is shown as the solid curve. Chosen filter cutoff period for the R/P *FLIP* vertical acceleration was 40 s.

riod for the vertical acceleration was 40 s, and a longer period (80 s) was used for the horizontal accelerations to account for low-frequency rotation of *FLIP* about its vertical axis. We note that E98 used the same filter cutoff for the three acceleration components. To verify our choice of accelerometer filter cutoff periods, the calculated platform velocity was integrated to obtain the platform displacement at the end of the portside boom (Fig. 2). We compared the calculated displacement with that expected for pitch and roll of *FLIP* about its center of mass (approximately 35 m below the ocean surface). During high wave conditions with relatively large motion, the range of vertical displacements was less than 1 m. For filter cutoff periods greater than 40 s, the calculated range of vertical displacement at the end of the portside boom increased linearly, consistent with the amplification of low-frequency accelerometer drift (Fig. 2).

d. Instrument-mounting offsets

The true mean vertical wind component \bar{w} in the surface layer was expected to be close to zero; however, at all levels the measured velocity along the z axis of the sonic anemometer \bar{w}_a was nonzero and increased in magnitude with horizontal wind speed (Fig. 3, gray x's). Two mechanisms could have produced this result: 1) the anemometers were tilted with respect to a horizontal plane such that horizontal wind components affected apparent wind along the anemometer z axis; and 2) the airflow was distorted by *FLIP*, the portside boom, the instrument mast, and/or the instrument

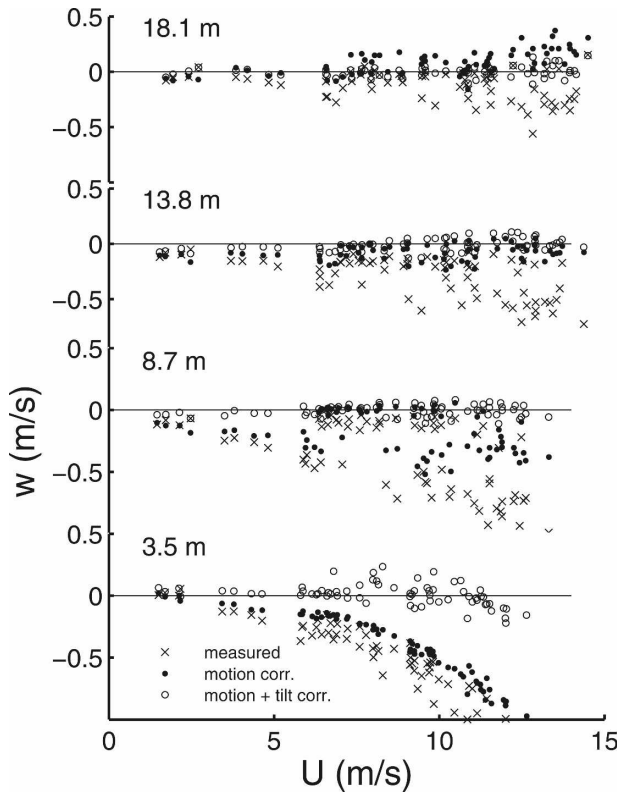


FIG. 3. The 30-min mean vertical velocity at four heights above the mean ocean surface measured from R/P *FLIP* vs wind speed: measured (x), motion corrected without accounting for anemometer-mounting offset angles (filled circles), and motion corrected including the anemometer-mounting offsets (open circles). Anemometer levels are indicated in the figure.

mounts (Yelland et al. 2002). The horizontal distance between the mast and *FLIP*'s hull was 20 m, more than 2.5 times *FLIP*'s widest horizontal dimension. This relatively large separation suggests that flow distortion due to the portside boom would have a greater impact on the airflow at the location of the mast (Mollo-Christensen 1979). However, the measured z component of the wind was negative at all levels, whereas flow distortion about the portside boom would be expected to deflect the flow in opposite directions for levels above, versus below, the boom. Based on these observations and the three-point mooring that maintained optimal exposure of the instrument mast, we conclude that the effect of anemometer tilting was likely the primary cause of nonzero wind components along the anemometer z axes.

The first attempt at applying motion correction to the *FLIP* dataset resulted in *corrected* mean vertical winds of order $10\text{--}100\text{ cm s}^{-1}$ during high wind periods (Fig. 3, solid dots). This suggested mounting offsets of each of the anemometers with respect to the motion sensor.

One source of alignment offset between the sonic anemometers and the motion sensor was caused by non-orthogonality between the top face of the port-side boom (on which the motion sensor was mounted) and the hinge mechanism to which the vertical mast was attached. In addition, at one point during the experiment waves struck the bottom of the mast and caused a relative shift in the mounting offsets between the motion sensor and anemometers. Finally, the mounting braces used to attach the anemometers to the mast were modified during setup to avoid interference with guy wires supporting the port boom during rotation of the mast from horizontal to vertical. This modification added uncertainty in the mounting orientation of the anemometers relative to the mast and motion sensor.

The complementary filter described in section 2c accounted for tilting of the motion sensor with respect to earth but did not account for mounting offsets of the anemometers with respect to the motion sensor. We define a transformation \mathbf{M}_{pa} as the relative mounting offset between an anemometer and the motion sensor. Compared to the transformation \mathbf{T} that is updated at the sampling rate of the turbulence and motion sensors (5 Hz for this dataset), the transformation \mathbf{M} is fixed and only changed if the relative offset between the anemometer and motion sensors changed, for example, after the mast was struck by waves. The transformation \mathbf{T}_{ea} in Eq. (3) was rewritten in terms of \mathbf{T}_{ep} according to $\mathbf{T}_{ea} = \mathbf{T}_{ep}\mathbf{M}_{pa}$,

$$\mathbf{u} = \mathbf{T}_{ep}\mathbf{M}_{pa}\mathbf{u}_a + \mathbf{T}_{ep}\left(\int \ddot{\mathbf{x}}_p dt + \boldsymbol{\Omega}_p \times \mathbf{r}_p\right) + \mathbf{v}_{\text{ship}}. \quad (4)$$

In E98, the motion sensor and anemometer were mounted together so their coordinate axes were coaligned and $\mathbf{M}_{pa} = \mathbf{I}$, where \mathbf{I} is the identity matrix. For the small offset angles we measured (less than 7° , Table 2), we found that the matrix multiplication $\mathbf{T}_{ea} = \mathbf{T}_{ep}\mathbf{M}_{pa}$ in Eq. (4) was closely approximated by simply adding the offset angles to the calculated Euler angles, that is, $\mathbf{T}_{ep}\mathbf{M}_{pa} = [\psi_{ep}][\theta_{ep}][\varphi_{ep}]\mathbf{M}_{pa} \approx [\psi_{ep}][\theta_{ep} + (\bar{\theta}_{ep} - \bar{\theta}_{ea})][\varphi_{ep} + (\bar{\varphi}_{ep} - \bar{\varphi}_{ea})]$.

The mounting offset angles between anemometers and the motion sensor were estimated using measured acceleration and wind signals. The transformation \mathbf{M}_{pa} was separated into two transformations that were each estimated from the measured data, $\mathbf{M}_{pa} = \mathbf{M}_{ep}^{-1}\mathbf{M}_{ea}$, where \mathbf{M}_{ep} is a transformation from the motion sensor to the earth frame, and \mathbf{M}_{ea} is a transformation from the anemometer frame to the earth frame. We estimated \mathbf{M}_{ep}^{-1} by assuming that the long-term average horizontal acceleration was zero. With this assumption, nonzero measured mean horizontal accelerations were due to tilting of the motion sensor relative to vertical (i.e.,

gravity). We estimated \mathbf{M}_{ea} by assuming that the long-term mean vertical wind velocity over the ocean was zero (in the absence of flow distortion), and nonzero measured mean vertical wind was due to tilting of the anemometer relative to the horizontal plane. The calculations are similar to the “planar fit” method presented by Wilczak et al. (2001). Equivalent roll (φ_{ea})

and pitch (θ_{ea}) offset angles of each anemometer with respect to earth were calculated using a least squares regression on (long) records of measured 30-min mean velocity components ($\bar{u}_a, \bar{v}_a, \bar{w}_a$). The regression resulted in pitch and roll angles that minimized the mean vertical wind velocity over long intervals (days). The transformation \mathbf{M}_{ea} was calculated as

$$\mathbf{M}_{ea} = [\theta_{ea}][\phi_{ea}] = \begin{bmatrix} \cos\theta_{ea} & 0 & \sin\theta_{ea} \\ 0 & 1 & 0 \\ -\sin\theta_{ea} & 0 & \cos\theta_{ea} \end{bmatrix} \begin{bmatrix} 1 & 0 & 0 \\ 0 & \cos\phi_{ea} & -\sin\phi_{ea} \\ 0 & \sin\phi_{ea} & \cos\phi_{ea} \end{bmatrix} = \begin{bmatrix} \cos\theta_{ea} & \sin\phi_{ea} \sin\theta_{ea} & \cos\phi_{ea} \sin\theta_{ea} \\ 0 & \cos\phi_{ea} & -\sin\phi_{ea} \\ -\sin\theta_{ea} & \sin\phi_{ea} \cos\theta_{ea} & \cos\phi_{ea} \cos\theta_{ea} \end{bmatrix}. \quad (5)$$

A similar approach was used to calculate \mathbf{M}_{ep} using long records of the 30-min-averaged measured acceleration components.

The calculated motion sensor and anemometer mounting offset angles relative to earth are shown in Table 2. The offset angles for the anemometers mounted to the mast were less than $\pm 4^\circ$. It was necessary to calculate the offset angles for two distinct periods, one before and the other after the mast was struck by high waves (Table 2).

e. Summary of correction algorithm

For the FLIP dataset, the mounting offset angles for the motion sensor ($\varphi_{ep}, \theta_{ep}$) and for each anemometer ($\varphi_{ea}, \theta_{ea}$) were calculated in a preprocessing step using 30-min-averaged measured wind speed and acceleration over the entire dataset. A single estimate of the offset angles was calculated by linear regression using all of the data during a period when the mean offset angles did not change. A step-change in the offset angles was clear after the mast was struck by waves. The offset angles calculated separately for the period before and after waves struck the mast are shown in Table 2. The offset angles of the 3.5-m sonic fixed to the pole were dependent on wind speed due to wind drag on the pole, and its offset angles were updated more frequently [thus, the nonlinear relationship between \bar{u} and \bar{w} in Fig. 3 (bottom)]. For this anemometer, a continuous time series of offset angles was generated using a sliding window: for each time period, forty-eight 30-min intervals nearest to the interval were used to calculate the offset angles. The resulting time series was smoothed with a running mean filter. For this sensor, the average of the time series before and after the mast was struck by waves is shown in Table 2.

The offset angles of the motion sensor and each anemometer were used to calculate the fixed transformation matrices \mathbf{M}_{ep} , \mathbf{M}_{ea} , and \mathbf{M}_{pa} according to the pro-

cedure in section 2d. For each flux interval, the “fast” transformation matrix \mathbf{T}_{ep} was calculated as outlined in section 2c and described in detail in E98. The remaining terms in Eq. (4) were measured. For the R/V *Wecoma* data, the anemometer and motion sensor were rigidly mounted with coaligned coordinate axes (as in E98), such that the preprocessing step was unnecessary.

After motion correction and before calculating turbulence statistics, with or without mounting offset angles, the wind vector was rotated into the 30-min mean wind direction such that the mean v and w components were zero (Donelan 1990). This rotation into the streamline (or “natural”) coordinate does not correct for motion effects but does affect turbulence statistics. We evaluate the effect of the mounting angle offsets on the turbulence statistics by comparing results calculated in the natural coordinate frame using $\mathbf{M}_{pa} = \mathbf{M}_{ep}^{-1}\mathbf{M}_{ea}$ and results calculated using $\mathbf{M}_{pa} = \mathbf{I}$.

3. Results

a. Mean vertical wind

Our first attempt at motion correction applied Eq. (4) and assumed that $\mathbf{M}_{pa} = \mathbf{I}$; that is, it accounted only for the orientation of the motion sensor with respect to earth, not for mounting offsets between the anemometer and motion sensor coordinate frames. The “corrected” vertical wind without accounting for mounting offsets also showed significant nonzero \bar{w} at all levels (Fig. 3, solid dots). We then calculated the mean mounting offsets (\mathbf{M}_{pa}) according to the procedure in section 2e and recalculated the motion correction according to Eq. (4). With the mounting offsets taken into account, the mean vertical wind was effectively removed by the motion correction (Fig. 3, open circles). Residual mean vertical velocities were generally less than 10 cm s^{-1} at all levels. We note that \mathbf{M}_{pa} minimized \bar{w} over long periods (days) but did not require that the

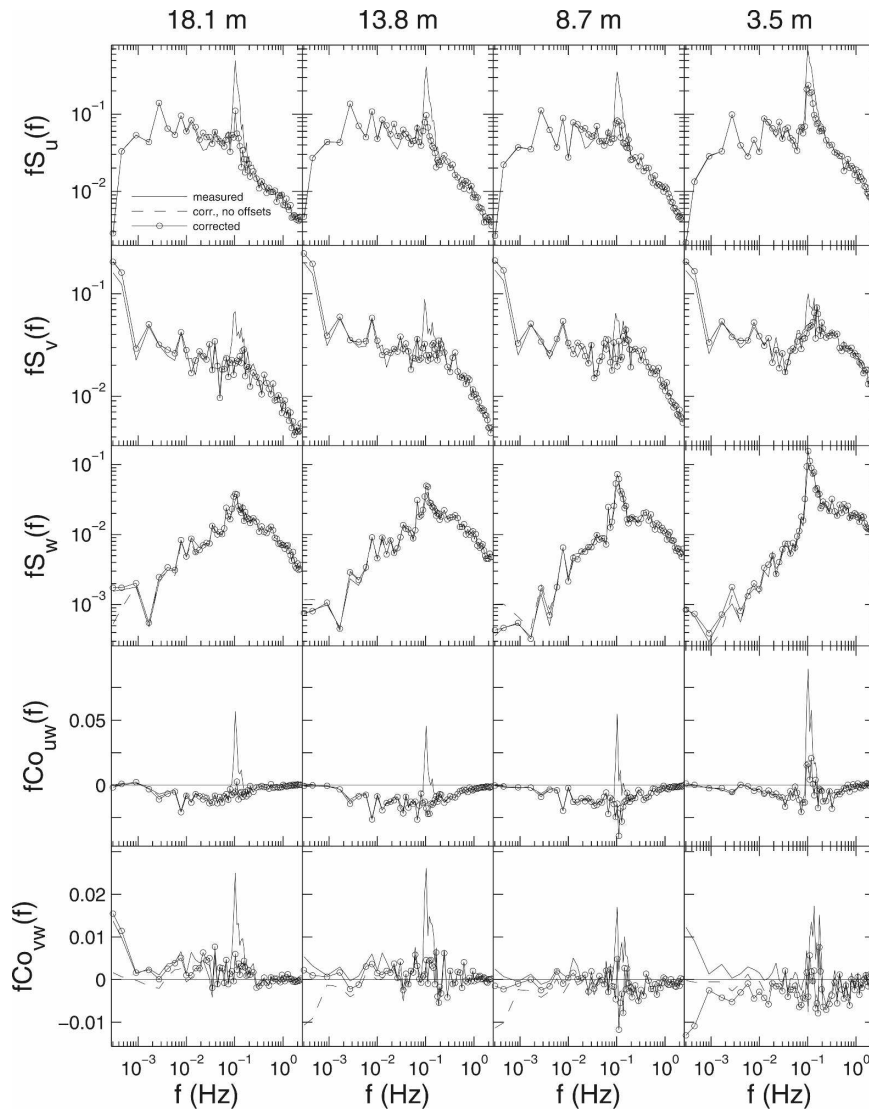


FIG. 4. Measured and motion-corrected velocity spectra and cospectra at four heights above the mean ocean surface measured from R/P *FLIP*. The mean 10-m wind speed was 7.3 m s^{-1} . Spectra and cospectra are frequency weighted and shown in natural coordinates: measured (solid curve), motion corrected without accounting for anemometer-mounting offset angles (dashed curve), and motion corrected including the anemometer-mounting offsets (solid curve with open circles). (row 1) Along-wind velocity component, u ; (row 2) crosswind velocity component, v ; (row 3) vertical velocity component, w ; (row 4) along-wind stress cospectrum, uw ; and (row 5) crosswind stress cospectrum, vw . Each column represents one of the four measurement levels: (column 1) 18.1 m; (column 2) 13.8 m; (column 3) 8.7 m; and (column 4) 3.5 m.

calculated vertical velocity for a 30-min interval be zero. As mentioned previously, an additional rotation into the natural coordinate frame for the flux record was performed before calculating turbulence statistics, such that $\bar{w} = \bar{v} = 0$ (Donelan 1990).

b. Effect of motion on spectra

Measured and motion-corrected velocity spectra and cospectra are shown for the four levels in Fig. 4 for a

60-min interval with moderate wind speed (7 m s^{-1} at 8.7-m height). Spectral peaks at the surface wave period (5–15 s) were found in the measured u - and v -component spectra (Fig. 4, solid curve in rows 1 and 2). The u and v spectral peaks were reduced by the motion correction at all levels, particularly 8.7, 13.8, and 18.1 m (solid curve with circles). The peaks at the lowest level were only partially removed by motion correction, suggesting real wind fluctuations near the sea surface cor-

TABLE 3. Effect of motion correction on turbulence statistics. First column is the average error magnitude (unsigned) combining the four sensors, calculated as $[(x - x_c/x_c) - 1]100$, where x is the measured statistic or corrected statistic without accounting for sensor-mounting offset angles, and x_c is the corrected statistic. Remaining columns are signed ratios x/x_c . Wind stress results are shown comparing measured stress to corrected stress (“measured”) and comparing corrections without accounting for sensor-mounting offsets to corrected stress (“no sensor tilt correction”). Data include 270 30-min samples collected over 6 days when 10-m wind speed varied between 1.1 and 13.3 m s^{-1} (mean 8.7 m s^{-1}). Errors are 95% confidence intervals.

	All levels (Error magnitude, %)	18.1-m ratio	13.8-m ratio	8.7-m ratio	3.5-m ratio
u variance (measured)	5 ± 0.3	1.02 ± 0.008	1.01 ± 0.008	1.01 ± 0.008	1.05 ± 0.009
v variance (measured)	15 ± 0.6	1.17 ± 0.019	1.14 ± 0.016	1.13 ± 0.015	1.10 ± 0.011
w variance (measured)	3 ± 0.1	1.01 ± 0.002	1.02 ± 0.002	1.03 ± 0.002	1.02 ± 0.004
Wind stress (measured)	15 ± 0.8	0.85 ± 0.02	0.87 ± 0.02	0.89 ± 0.02	1.03 ± 0.03
Wind stress (no sensor tilt correction)	5 ± 0.3	0.93 ± 0.01	0.98 ± 0.004	0.98 ± 0.004	1.03 ± 0.01

related with the surface waves (e.g., Hristov et al. 2003). The w -component spectra support the presence of wave-correlated fluctuations, as the corrected spectral peak at the surface wave period was largest at the lowest level and decreased with distance from the surface (Fig. 4, row 3). Compared to the u and v components, the motion correction had little effect on the vertical velocity spectrum, presumably because *FLIP*'s stability minimized platform vertical velocity.

The uncorrected along-wind stress cospectra were negative at all four levels corresponding to downward momentum transfer, except for a sharp positive peak at the surface wave frequency (Fig. 4, row 4). The motion correction removed most of these peaks. For this interval, the motion correction had little effect at high and low ends of the cospectrum. The uncorrected crosswind stress cospectra also showed peaks at the surface wave frequency (Fig. 4, row 5). The motion correction removed most of these peaks, and the corrected crosswind cospectra were close to zero.

The mean tilt angle correction had negligible effect on velocity spectra and cospectra at the surface wave and higher frequencies during the interval shown in Fig. 4 (dashed curves). The mean tilt correction had a small effect on the low-frequency vertical power spectrum and a larger effect on the low-frequency uw cospectra. The net effect of the mean sonic tilt angle correction on velocity variances and covariances is discussed below.

c. Wind velocity variances and covariances

The effect of motion corrections on velocity variances is expressed as $\sigma_{\text{meas}}^2/\sigma_{\text{corr}}^2$, where σ_{meas}^2 is the measured variance and σ_{corr}^2 is the corrected variance. Table 3 summarizes the corrections for 6 days of measurements with the most favorable relative wind directions. The 10-m wind speed varied between 1 and 13 m s^{-1} . The average error magnitude was 5% for σ_u^2 , 15% for σ_v^2 , and 3% for σ_w^2 . The insensitivity of σ_w^2 to

motion was presumably due to the stability of *FLIP*. The signed average error was less for the individual levels (Table 3). The correction to σ_v^2 showed a systematic dependence on measurement height, while σ_u^2 and σ_w^2 did not. The measured σ_v^2 was overestimated by 18% at the 18-m level and decreased to 10% at the 3.5-m level. The effect of mean sensor tilt had a negligible (<1%) effect on each of the velocity component variances.

The velocity variance correction showed a different dependence on the 10-m wind speed for each of the wind components (Fig. 5). The shapes of the curves in Fig. 5 were similar when plotted against *FLIP*'s motion, calculated as the difference between the maximum and minimum Euler angles in a 30-min flux record ($\Delta\phi$, $\Delta\theta$, or $\Delta\psi$). Regressions between wind speed and motion were as follows: $\Delta\phi = 0.02 U_{10}^2 - 0.02 U_{10} + 1$, $r^2 = 0.39$; $\Delta\theta = 0.07 U_{10}^2 - 0.6 U_{10} + 2.3$, $r^2 = 0.5$; and $\Delta\psi = 0.07 U_{10}^2 + 0.2 U_{10} + 0.7$, $r^2 = 0.89$. The measured σ_u^2 was overestimated by approximately 15% for wind speeds less than 6 m s^{-1} . Above 6 m s^{-1} , σ_u^2 was less than 5% and was not wind speed or motion dependent (Fig. 5, top). In contrast, the measured error in σ_v^2 was smallest for wind speeds between 6 and 8 m s^{-1} and was larger for higher and lower wind speeds. The σ_v^2 correction showed a systematic height dependence for wind speeds above 8 m s^{-1} , with larger errors at the higher measurement levels (Fig. 5, middle). The motion correction to σ_w^2 was small across all wind speed values and all measurement heights (Fig. 5, bottom).

Combining the four measurement levels, the average magnitude of wind stress error for 270 30-min intervals (10-m wind speed range 2–14 m s^{-1}) was 15% \pm 1% (Table 3). Without accounting for sensor tilt offsets, the error average magnitude was 5%, indicating that one-third of the wind stress correction was associated with the angle offsets. The signed average error at each level showed a systematic dependence on measurement

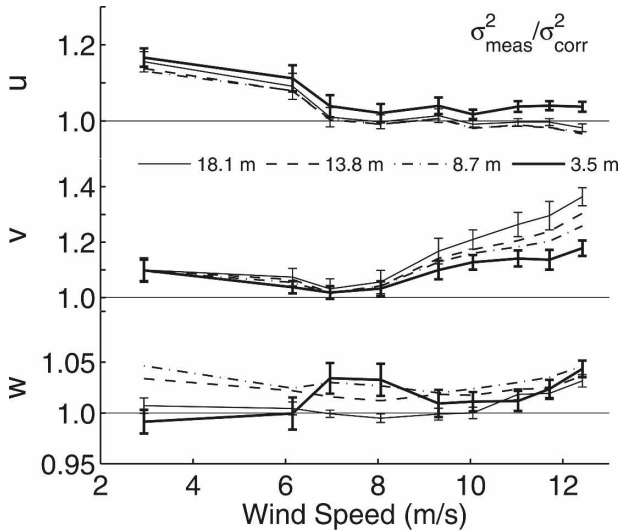


FIG. 5. Effect of motion correction on velocity variances measured from R/P *FLIP* vs 10-m wind speed: 18.1 m (solid, thin), 13.8 m (dash), 8.7 m (dash-dot), and 3.5 m (solid, thick). Regressions between wind speed and the magnitude of *FLIP*'s pitch, roll, and yaw motion are given in the text. (top) Along-wind velocity, (middle) crosswind velocity, and (bottom) vertical velocity. Error bars showing the 95% confidence intervals are included for the highest and lowest anemometer levels.

height (Table 3 and Fig. 6). On average, the measured wind stress was underestimated by $15\% \pm 2\%$ (95% confidence interval) at 18.1 m, $13\% \pm 2\%$ at 13.8 m, and $11\% \pm 2\%$ at 8.7 m, and overestimated by $3\% \pm 3\%$ at 3.5 m. Thus, the motion correction modified the wind stress profile, shifting wind stress to higher values at the upper levels and lower values at the near-surface level. The contribution of platform motion to the stress error was larger during high-wind periods (with more platform motion; Fig. 6a). The contribution of sensor-mounting offsets to wind stress error was largest at the lowest and highest levels (Fig. 6b).

Motion correction had a large effect on the crosswind stress $-\overline{v'w'}$. The measured crosswind stress was generally negative and proportional to wind stress, and the corrected crosswind stress was close to zero, though the scatter remained large (Fig. 7). We calculated the wind stress “angle” using the along-wind and crosswind stress components, $\alpha \equiv \tan^{-1}(-\overline{v'w'}/-\overline{u'w'})$, which some studies have linked to interactions between the surface wave and wind fields (Rieder et al. 1994; Friehe et al. 2001; Grachev et al. 2003). The motion correction reduced the measured wind stress angle at all levels (Fig. 7, dashed curves compared to solid curves). The sensitivity of the stress angle to motion correction, even for the small amounts of motion on *FLIP*, suggests caution when calculating this quantity from measured data.

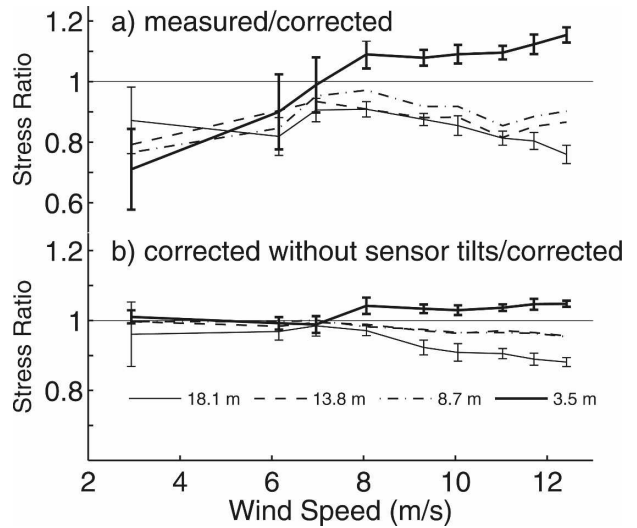


FIG. 6. Effect of motion correction on wind stress: (a) ratio of measured wind stress to corrected stress and (b) ratio of corrected stress without accounting for sensor tilts to the corrected stress.

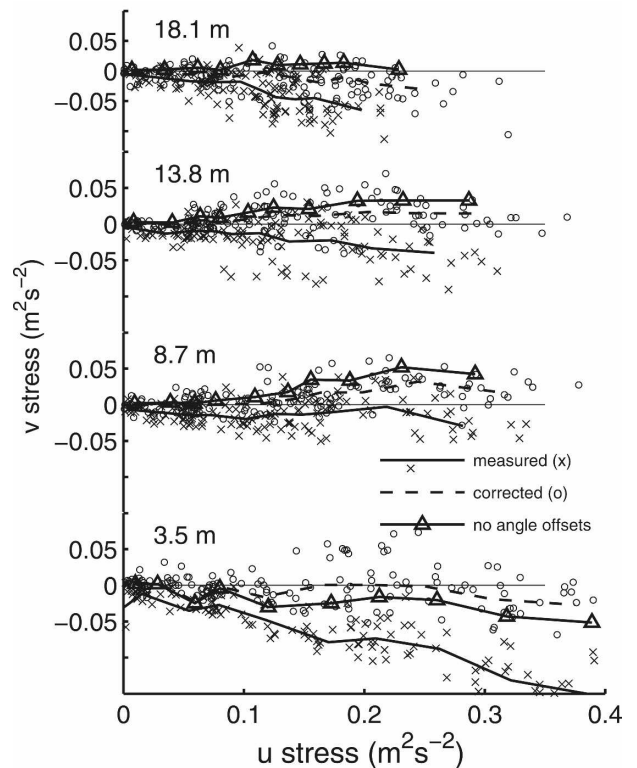


FIG. 7. Effect of motion correction on crosswind stress covariance $-\overline{v'w'}$ vs along-wind stress covariance $-\overline{u'w'}$ measured from R/P *FLIP*: solid curve and x's are measured data, dashed curve and open circles are motion corrected including sensor-mounting offsets, and solid curve with triangles is motion corrected without including sensor offsets. Measurement heights are indicated in the figure.

d. Contribution of linear versus angular motion to wind stress error

We analyzed the relative importance of the three terms of the motion correction in Eq. (4) to the along-wind stress: the effect of rotating the measured velocity vector (coordinate rotation term) $\mathbf{T}_{ep}\mathbf{M}_{pa}\mathbf{u}_a$; the effect of platform linear velocity $\int \mathbf{T}_{ep}\ddot{\mathbf{x}}_p dt$; and the effect of angular motions $\mathbf{T}_{ep}(\boldsymbol{\Omega}_p \times \mathbf{r}_p)$. Similar to previous studies (E98, Schulz et al. 2005), the angular contribution was negligible compared to the other two terms. In our data, this was due to the small angle rates and the relatively small distance (\mathbf{r}_p) between the motion sensor and anemometers. For the lowest wind conditions and small waves, the linear platform motions contributed over 90% of the total motion correction to wind stress. In contrast, during the highest wind and wave conditions, the coordinate rotation term was larger, accounting for ~75% of the stress correction. The shift of the motion correction from the linear to coordinate rotation terms resulted from increased pitching and rolling and more cross contamination of w by u and v during the higher wind and seas states.

e. Motion correction of winds measured from R/P FLIP versus a conventional ship

We compared the effect of platform motion on wind and wind stress measured at the 8.7-m level from *FLIP* with in situ measurements from a conventional research ship, the *R/V Wecoma*. Results are shown for a 3-day overlap period when the average 10-m wind speed was 6.4 m s^{-1} , the average distance between *Wecoma* and *FLIP* was 10 km (maximum 42 km), and the relative wind direction for each platform was within $\pm 60^\circ$ of forward (Fig. 8). For the *Wecoma* data, the motion correction resulted in a sign change of the stress from negative (measured) to positive (corrected) for 56% of the periods during the overlap interval. The magnitude of the stress correction as a fraction of the corrected stress for *Wecoma* was $77\% \pm 22\%$, compared to only $4\% \pm 2\%$ for *FLIP* during the overlap period. The stability of *FLIP* due to its 100 m of draft results in much less pitching and rolling than conventional ships. Vertical motion on *FLIP* is also highly damped, with platform vertical motions of order centimeters per second, compared to conventional ships where vertical motions are routinely of order meters per second, particularly at the ship’s bow, where wind turbulence sensors are typically mounted.

4. Discussion and conclusions

The mounting offsets between the motion sensor and anemometers contributed to one-third of the total mo-

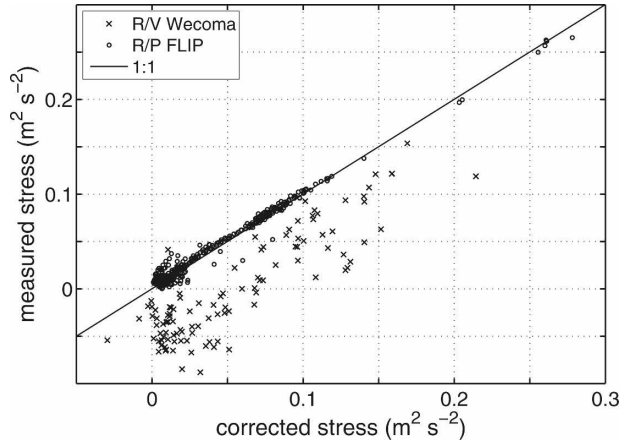


FIG. 8. Effect of motion correction on wind stress measured from R/P *FLIP* and from R/V *Wecoma*. The data were collected in situ during the MBL experiment in 1995, 50 km off the coast of Monterey, CA. R/P *FLIP* wind stress measured at 8.7-m height and calculated from 30-min data records. R/V *Wecoma* wind stress measured at 10-m height and calculated from 10-min records.

tion correction to the wind stress over all periods (Fig. 6). This source of error has not been considered previously but should be accounted for when the two sensors are not coaligned. When feasible, it is recommended to use mounting arrangements whereby the relative orientations of the motion sensor and anemometer are coaligned and fixed (e.g., E98). This may not be possible when the motion is measured by a distributed set of sensors (e.g., Song et al. 1996, Schulz et al. 2005) or when a single motion sensor is used to correct several anemometers, as in this study. In this case, the method presented in this paper based on measured wind and motion data may provide a means to account for differences between motion sensor and anemometer orientation.

The motion correction had qualitative effects relevant to air–sea interaction, as it removed much of the features in the wind spectra and cospectra at the wave frequency. However, remaining signal at the wave frequency likely contains real interaction between the wind and surface waves. The motion-corrected u and w spectra showed peaks correlated with the surface wave field that were most apparent at the near-surface level yet could be seen at all levels to 18.1 m, with the wave-correlated peak decaying with distance from the surface (Fig. 4). During the low-wind conditions, the motion-corrected uw cospectrum at 3.5 m indicated upward transfer of momentum at the wave frequency, similar to that reported by Grachev and Fairall (2001). The motion correction also had a large impact on the apparent angle between the wind and wind stress vector. We found a marked reduction in the angle at all levels after

the wind vector was corrected for platform motion due to the motion sensitivity of the crosswind stress (Fig. 7).

The increased importance of pitch and roll relative to linear motions as platform motion increased, and the larger wind stress error during higher wind (Fig. 6), suggest more uncertainty in wind stress estimates during high wind and wave states. These conditions represent a critically important, yet relatively undersampled, regime. Whereas strapped-down motion measurement systems offer several significant advantages (e.g., low cost, rugged, easier to employ), gyro-stabilized systems may provide some benefit in situations with considerable pitching and rolling, such as conventional research vessels measuring in high sea states.

FLIP's stability and the ability to deploy a mast relatively far from the hull are advantageous for making turbulence measurements compared to conventional ships, and corrections to the along-wind and vertical velocity variances were small in this dataset (Table 3). The effect of motion on wind stress was larger and showed a surprising amount of variability among anemometers separated by less than 20 m. This result reflects the complexity of the interaction between the motion of the platform and the turbulent wind, and reinforces the need to measure and carefully correct the measured wind vector for the contamination caused by platform motion.

Acknowledgments. We thank Matt Shumway, Patrick Hong, and Peter Gulcher of UCI; George Trekas of the Scripps Marine Physical Lab; and Captain Tom Golfinos, Bill Gaines, and the crew of the R/P *FLIP* for their assistance. The comments of two anonymous reviewers helped to improve the manuscript. This research was funded by ONR. TSH, acknowledges support from ONR N00014-06-11017.

REFERENCES

- Ancil, F., M. A. Donelan, W. M. Drennan, and H. Graber, 1994: Eddy-correlation measurements of air-sea fluxes from a discus buoy. *J. Atmos. Oceanic Technol.*, **11**, 1144–1150.
- Donelan, M. A., 1990. Air-sea interaction. *The Sea*, B. LeMehaute and D. M. Hanes, Eds., Ocean Engineering Science, Vol. 9 Wiley and Sons, 239–292.
- Drennan, W. M., H. C. Graber, and M. A. Donelan, 1999: Evidence for the effects of swell and unsteady winds on marine wind stress. *J. Phys. Oceanogr.*, **29**, 1853–1864.
- Dugan, J. P., S. L. Panichas, and R. L. DiMarco, 1991: Decontamination of wind measurements from buoys subject to motions in a seaway. *J. Atmos. Oceanic Technol.*, **8**, 85–95.
- Dunckel, M., L. Hasse, L. Krugermeyer, D. Schriever, and J. Wucknitz, 1974: Turbulent fluxes of momentum, heat and water vapor in the atmospheric surface layer at sea during ATEX. *Bound.-Layer Meteor.*, **6**, 81–106.
- Edson, J. B., A. A. Hinton, K. E. Prada, J. E. Hare, and C. W. Fairall, 1998: Direct covariance flux estimates from mobile platforms at sea. *J. Atmos. Oceanic Technol.*, **15**, 547–562.
- Friehe, C. A., J. A. Smith, K. F. Rieder, N. E. Huang, J.-P. Giovanangeli, and G. L. Geernaert, 2001: Wind, stress and wave directions. *Wind Stress over the Ocean*, I. S. F. Jones and Y. Toba, Eds., Cambridge University Press, 232–241.
- Fujitani, T., 1985: Method of turbulent flux measurement on a ship by using a stable platform system. *Pap. Meteor. Geophys.*, **36**, 157–170.
- Geernaert, G. L., F. Hansen, M. Courtney, and T. Herbers, 1993: Directional attributes of the ocean surface wind stress vector. *J. Geophys. Res.*, **98**, 16 571–16 582.
- Grachev, A. A., and C. W. Fairall, 2001: Upward momentum transfer in the marine boundary layer. *J. Phys. Oceanogr.*, **31**, 1698–1711.
- , —, J. E. Hare, J. B. Edson, and S. D. Miller, 2003: Wind stress vector over ocean waves. *J. Phys. Oceanogr.*, **33**, 2408–2429.
- Hristov, T. S., S. D. Miller, and C. A. Friehe, 2003: Dynamical coupling of wind and ocean waves through wave-induced air flow. *Nature*, **422**, 55–58.
- Leavitt, E., and C. A. Paulson, 1975: Statistics of surface layer turbulence over the tropical ocean. *J. Phys. Oceanogr.*, **5**, 143–156.
- Mollo-Christensen, E., 1979: Upwind distortion due to probe support in boundary layer observation. *J. Appl. Meteor.*, **18**, 367–370.
- Oppenheim, A. V., and R. W. Schaffer, 1989: *Discrete-Time Signal Processing*. Prentice Hall, 879 pp.
- Rieder, K. F., J. A. Smith, and R. A. Weller, 1994: Observed directional characteristics of the wind, wind stress and surface waves on the open ocean. *J. Geophys. Res.*, **99**, 22 589–22 596.
- Rudnick, P., 1967: Motion of a large spar buoy in sea waves. *J. Ship Res.*, **11**, 257–267.
- Schmitt, K. F., C. A. Friehe, and C. H. Gibson, 1979: Structure of marine surface layer turbulence. *J. Atmos. Sci.*, **36**, 602–618.
- Schulz, E. W., B. G. Sanderson, and E. F. Bradley, 2005: Motion correction for shipborne turbulence sensors. *J. Atmos. Oceanic Technol.*, **22**, 55–69.
- Song, X., C. A. Friehe, and D. Hu, 1996: Ship-board measurements and estimations of air-sea fluxes in the western tropical Pacific during TOGA-COARE. *Bound.-Layer Meteor.*, **81**, 373–397.
- Vickers, D., and L. Mahrt, 2006: Contrasting mean vertical motion from tilt correction methods and mass continuity. *Agric. For. Meteorol.*, **138**, 93–103.
- Wilczak, J., S. Oncley, and S. Stage, 2001: Sonic anemometer tilt correction algorithms. *Bound.-Layer Meteorol.*, **99**, 127–150.
- Yelland, M., B. I. Moat, R. W. Pascal, and D. I. Berry, 2002: CFD model estimates of the airflow distortion over research ships and the impact on momentum flux measurements. *J. Atmos. Oceanic Technol.*, **19**, 1477–1499.